

Metal–Polymer–Metal Split-Dipole Nanoantennas

Deirdre M. O'Carroll,* James S. Fakonias, Dennis M. Callahan, Martin Schierhorn, and Harry A. Atwater

The ability to modify semiconductor optical properties using nanostructures that support surface plasmon resonances has enabled the demonstration of improved light-management in conventional opto-electronic devices, such as light-emitting diodes,^[1–3] lasers,^[4] and photovoltaic devices,^[5,6] as well as in integrated optical computing and light localization on the nanoscale.^[7–11] In particular, resonant plasmonic nanoantennas can be used to control the polarization, directivity, light-emission intensity and decay rate of coupled emitters via the large local density of optical states in the nanoantenna's near-field.^[7–16] Recent theoretical studies have proposed linear metal–semiconductor–metal nanoantennas where semiconductor material is incorporated into a central 'slot region' of a noble metal nanorod, in analogy to the feed element in radio frequency antennas.^[11,17] This not only allows the full benefit of local-field effects in the antenna near-field to be exploited, but also permits light to be efficiently in/out coupled to sub-wavelength semiconductor material volumes. However, realizing integrated metal–semiconductor nanoantenna structures such as these remains challenging. Additionally, the application of plasmonic nanoantennas to organic semiconductor materials for improved light management has been largely unexplored despite the potential for enhancing emission rate and quantum efficiency. In particular, organic conjugated polymer semiconductors such as polythiophene, which exhibit high carrier mobilities but possess relatively poor luminescence properties,^[18–20] would benefit from plasmonic nanoantennas, potentially opening up opportunities for use as the active material in organic light-emitting optoelectronic devices.

Here, we integrate the conjugated polymer semiconductor poly(3-hexylthiophene), P3HT, directly into the slot region of resonant plasmonic split-dipole nanoantennas. Using this approach, P3HT radiative emission rate is enhanced by a factor of up to 29, in experiment, and 550 for the ideal case (theory). Additionally, theoretical modified luminescence quantum efficiency is shown to increase from 1% up to 45% for optimized nanoantenna parameters. This work demonstrates that integrated metal–polymer–metal nanoantennas could enable a new generation of high-performance conjugated polymer optoelectronic devices.

The split-dipole nanoantennas are comprised of two gold nanorods bridged by P3HT as illustrated in **Figure 1a**. The resonant scattering response of the entire antenna can be tuned to the P3HT emission band (650–750 nm) by controlling the nanoantenna length, L .^[11,17] To observe the antenna electric-field profiles, full-field finite-difference-time-domain (FDTD) electromagnetic simulations were carried out for the structure with a P3HT slot height, s , of 20 nm and nanoantenna diameter, d , of 60 nm under plane wave excitation (free-space wavelength of 700 nm; background refractive index, n_{bk} , was 1.48). **Figure 1a** shows the electric-field intensity profiles for split-dipole nanoantennas at resonance lengths of 180, 440, and 780 nm, corresponding to half-wave and higher order resonances (Supporting Information (SI), **Figure S1**). Clearly, the field intensity was strongly confined to the P3HT slot region of the nanoantenna with intensity enhancements of up to 150. To simulate an excited P3HT molecular segment, a dipole excitation source, oriented parallel to the nanoantenna long axis, was placed in the P3HT slot region and values for the total decay rate, Γ_t , and the radiative decay rate, Γ_r , were extracted (calculated values of total and radiative decay rates from FDTD simulations were normalized to those of a dipole emitter in vacuum; see Experimental Section). The modified quantum efficiency of the dipole emitter in P3HT, η_m , was then calculated according to the expression:^[8–10,21,22]

$$\eta_m = \frac{\Gamma_r / \Gamma_r^0}{\Gamma_r / \Gamma_r^0 + \Gamma_{\text{nr}}^A / \Gamma_r^0 + (1 - \eta_0) / \eta_0} \quad (1)$$

where Γ_r^0 is the radiative decay rate in P3HT without the gold nanoantenna and η_0 is the intrinsic luminescence quantum efficiency of P3HT (~1%)^[19,20] which accounts for the large intrinsic non-radiative decay rate, Γ_{nr}^0 , associated with P3HT (i.e., $\Gamma_{\text{nr}}^0 = \Gamma_r^0(1 - \eta_0) / \eta_0$); see SI for derivation of Equation 1). **Figure 1b** is a plot of the enhancement in Γ_r and Γ_{nr}^A (relative to a dipole emitter in P3HT without the metal nanoantenna) and η_m for a range of nanoantenna lengths. While Γ_{nr}^A was relatively unchanged with nanoantenna length, Γ_r and η_m were enhanced by factors of 53 and 25, respectively, at the half-wave resonance due to an efficiently radiating nanoantenna and to a lesser degree at higher-order resonances.

Prof. D. M. O'Carroll

Department of Materials Science and Engineering/V
Rutgers University
607 Taylor Road, Piscataway, New Jersey 08854, USA
E-mail: ocarroll@rutgers.edu

Prof. D. M. O'Carroll

Department of Chemistry and Chemical Biology
Rutgers University
607 Taylor Road, Piscataway, New Jersey 08854, USA

J. S. Fakonias, D. M. Callahan, Prof. H. A. Atwater
Thomas J. Watson Sr. Laboratory of Applied Physics
California Institute of Technology
1200 East California Blvd., Pasadena, California 91125, USA

Dr. M. Schierhorn

Department of Chemistry and Biochemistry
University of California
Santa Barbara, California 93106, USA

DOI: 10.1002/adma.201103396



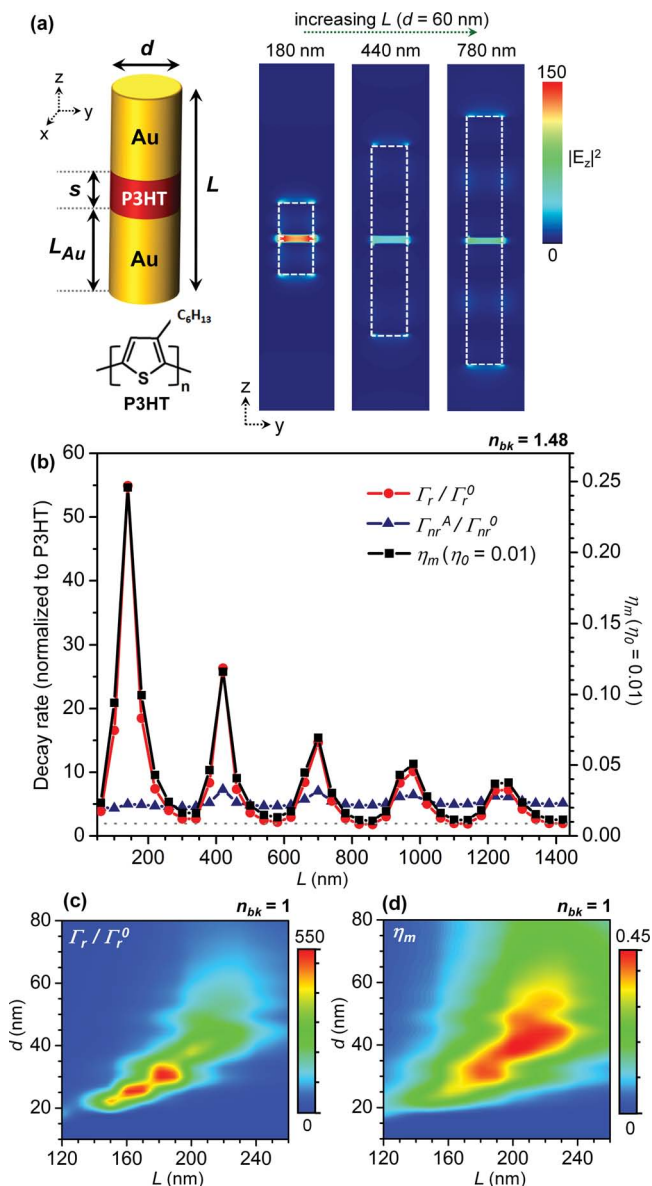


Figure 1. Theoretical design of resonant gold–polythiophene–gold split-dipole nanoantennas. a) Top left: Schematic of split-dipole plasmonic nanoantenna with P3HT in the slot region. Bottom left: Molecular structure of P3HT. Right panels: Theoretical 2D z-polarized electric-field intensity cross-sections through nanoantennas with different lengths. b) Theoretical radiative and non-radiative decay rate enhancement (relative to a dipole in P3HT in the absence of a nanoantenna) and modified quantum efficiency for a dipole emitter placed in the center of the P3HT slot region as a function of L (dipole oriented parallel to the nanoantenna long axis). c) Theoretical radiative decay rate and d) quantum efficiency enhancements as a function of L and d in the half-wave nanoantenna regime. All theoretical data was simulated using 3D full-field FDTD software using a free-space wavelength of 700 nm (see Experimental Section).

At optical frequencies, it is expected that the radiative efficiency of a nanoantenna depends not only on its length but also on its diameter.^[17] Figure 1c is a 3D plot of Γ_r / Γ_r^0 as function of d and L around the half-wave resonance of the nanoantenna (here $n_{bk} = 1$). Optimum enhancement in Γ_r , by a factor of 550,

occurred for $d = 27$ nm and $L = 180$ nm and η_m values of up to 45% were achievable for diameters in the range 28 to 45 nm and nanoantenna lengths between 180 and 230 nm. The diameter and length at which η_m was a maximum were larger than those for Γ_r due to a greater contribution of non-radiative decay rate enhancement for smaller diameters (Figure 1d). Therefore, nanoantennas that are designed to optimize quantum efficiency require slightly larger dimensions than antennas that are designed to optimize radiative decay rate. Although the simulations were carried out for a single dipole source placed in the center of the P3HT slot region, large enhancements were expected for dipoles positioned at other locations within the slot (SI, Figure S3). Therefore, in fabricated structures an ensemble of P3HT emitters in the slot region are expected to be modified by the nanoantenna.

Split-dipole nanoantenna heterostructures were fabricated using a template-directed sequential electrodeposition process followed by a metal evaporation step (Figure 2 and Experimental Section). The template employed was nanoporous alumina which was grown by anodizing 300–600 nm of aluminum on a conductive substrate (ITO or gold) in oxalic acid and subsequent pore widening (Figure 2a,b).^[23–25] Gold and P3HT were electrodeposited into the alumina template pores in sequence under pulsed potentiostatic conditions (Figure 2c,e). The height of the electrodeposited gold segments was varied between 20 and 150 nm across a given sample and the height of P3HT deposited on the gold segment was kept constant (typically at a value between 20 and 50 nm depending on the number of applied pulses). To complete the split-dipole nanoantenna structure, 40–80 nm of gold was evaporated through the alumina template onto the ends of the P3HT segments (Figure 2d). To ensure the gold was deposited into the template pores during this final step it was critical for the thickness of the template to be ≤ 600 nm. Multiple regions with nanoantennas of different lengths were fabricated on a single substrate by varying the deposition time of the gold segments within each region (Figure 2f).

Figure 3a and b show cross-sectional scanning electron microscopy (SEM) images of gold–P3HT–gold split-dipole nanoantennas after fabrication in an alumina template and after template removal, respectively. Typically, the fabricated nanoantennas exhibited rounded or cone-shaped gold segments on the top side due to shadowing by the template pore walls during the metal evaporation step (Figure 3a–d). Simulations of asymmetric split-dipole nanoantennas with one cone-shaped gold segment showed that, compared to symmetric nanoantennas with similar total length, the resonance wavelength of the nanoantenna did not change significantly, though electric-field intensity in the slot region decreased by a factor of ~ 2 (SI, Figure S4).

To detect longitudinal resonances of nanoantennas vertically oriented on the growth substrate, reflection spectra of arrays with different lengths were collected with objectives of different numerical aperture, n.a. (Figure 3e). The reflection spectrum of an array of nanoantennas with $L = 196 \pm 20$ nm collected with a 0.2 n.a. objective showed a broad minimum at 510 nm, which was attributed to transverse nanoantenna resonances. Reflection spectra acquired with a 0.65 n.a. objective allowed longitudinal antenna resonances to be more

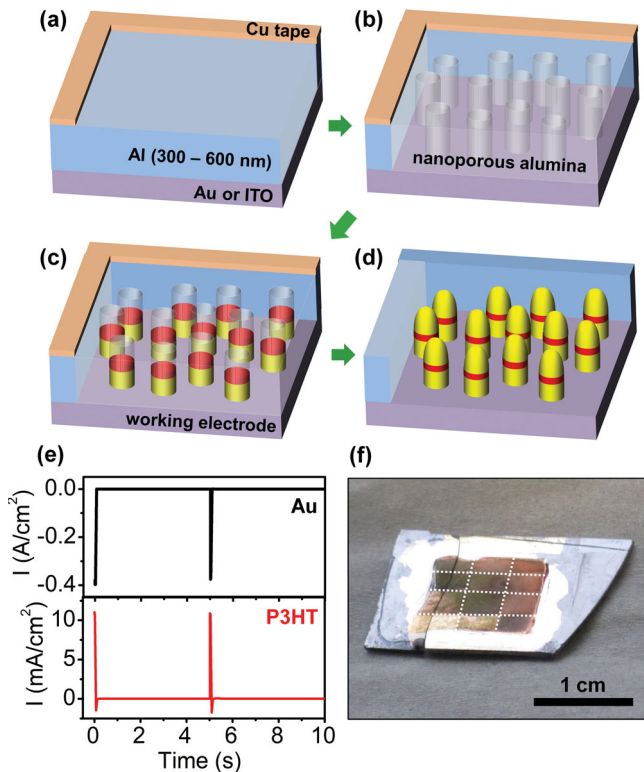


Figure 2. Schematics of the fabrication process for gold-P3HT-gold split-dipole nanoantenna heterostructures by sequential electrodeposition and thermal evaporation in nanoporous alumina templates on conductive substrates: a,b) 300–600 nm of aluminum on gold or ITO was anodized in oxalic acid at 35 V to form a supported, electrically contacted, nanoporous alumina template. Alumina grown in this way had cylindrical pores (55 nm in diameter) which were vertically oriented relative to the conductive substrate. c) Following a pore widening step and alumina barrier etch, gold and P3HT were electrodeposited within the template pores, sequentially. d) Nanoantenna fabrication was completed by thermally evaporating 40–80 nm of gold through the pores of the alumina template onto the P3HT segments. e) Typical current density versus time plots acquired during pulsed electrodeposition of gold and P3HT in nanoporous alumina templates. For gold deposition, -3 V pulses (versus a platinum mesh quasi-reference electrode, QRE) of 0.02 s duration were applied to the working electrode with -0.2 V applied for 5 s between pulses. For P3HT electrodeposition (electropolymerization from the 3HT monomer), $+3$ V pulses (versus Pt QRE) of 0.02 s duration were applied with -0.6 V for 5 s between pulses. f) A true-color photograph of a sample with twelve different regions with nanoantennas of different lengths (acquired at an angle of $\sim 50^\circ$ off-normal to the substrate plane under halogen lamp lighting; regions are delineated by white dashed lines).

effectively excited and collected and, as a result, an additional minimum was apparent in the reflected-light spectrum at ~ 670 nm. The differential extinction in an angular range of 11° to 35° off-normal incidence exhibited a pronounced peak at 690 nm (Figure 3f). In contrast, the differential extinction spectrum of a nanoantenna array with $L = 47 \pm 7$ nm did not show longitudinal resonances in the visible range of the spectrum. The scattered-light spectra from isolated nanoantennas with lengths in the 100–250 nm range exhibited narrow, pronounced resonances with peak maxima in the 600 to 800 nm wavelength range (Figure 3f, inset).

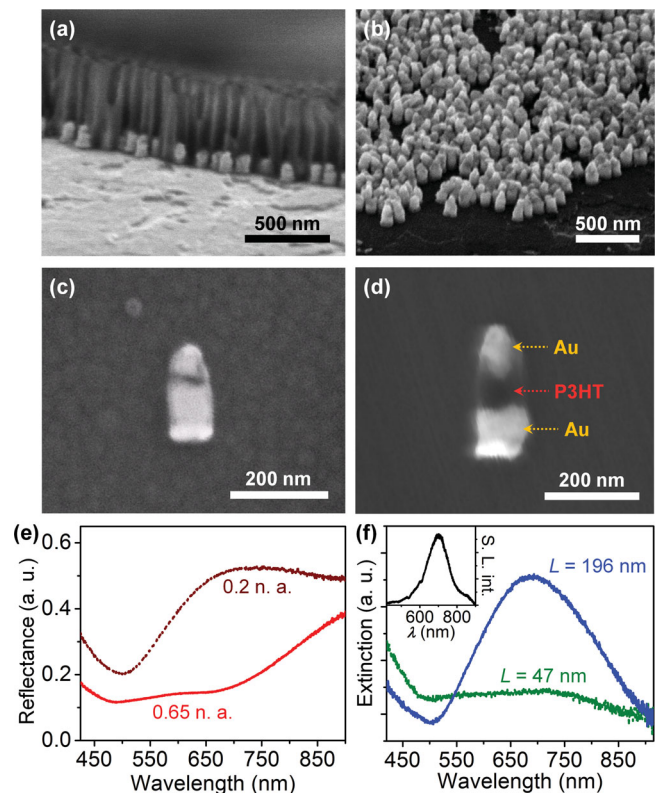


Figure 3. Cross-sectional SEM images of vertically oriented gold-P3HT-gold nanoantenna arrays a) in the alumina template and b) after alumina template removal (acquired at a 45° sample tilt). c,d): SEM images of single nanoantennas with different segment lengths (on gold and silicon substrates, respectively). e) Reflectance spectra of a vertically oriented array of nanoantennas with $L = 196 \pm 21$ nm acquired using a 0.2 n.a. objective and a 0.65 n.a. objective (relative to planar aluminum). f) Differential extinction spectra for arrays of nanoantennas with lengths of 47 ± 7 nm and 196 ± 21 nm (calculated from the reflectance spectra as $[(1-R_{0.65}) - (1-R_{0.2})]/(1-R_{0.2})$, where $R_{0.65}$ and $R_{0.2}$ are the reflection intensities from the nanoantenna arrays for the 0.65 n.a. and 0.2 n.a. objectives, respectively, relative to planar aluminum). Inset: Scattered-light spectrum of a single split-dipole nanoantenna ($L \sim 190$ nm) embedded in optical epoxy with refractive index of 1.48.

PL spectral intensity from nanoantenna arrays also exhibited a dependence on nanoantenna length, with PL enhancements, E_{PL} , increasing from less than a factor of 2, for $L = 82 \pm 9$ nm, up to a factor of 12, for $L = 116 \pm 16$ nm at 700 nm (Figure 4a and inset; $E_{\text{PL}} = I_{\text{PL}}/I_{\text{PL}}^0$, and I_{PL}^0 is the PL intensity for a $L = 47$ nm nanoantenna array; excitation wavelength, λ_{ex} , was 375 nm). E_{PL} values determined from total PL lifetime decay curves at time = 0 ps exhibited a similar trend with L (the total PL lifetime decay curves were acquired for the wavelength range 650–750 nm). Total PL lifetime, τ_{PL} , was determined from PL lifetime decay curves by least-squares fitting with a double exponential function and calculating the amplitude-weighted average lifetime using the fit parameters (see SI). τ_{PL} values for the nanoantennas ranged from 60 to 240 ps; Figure 4b, inset (the shorter lifetimes were likely to have been limited by the instrument response time of the PL lifetime system which was 52 ps). These values were significantly shorter than τ_{PL} values for neat P3HT thin films and nanowires (600 ± 40 ps and $720 \pm$

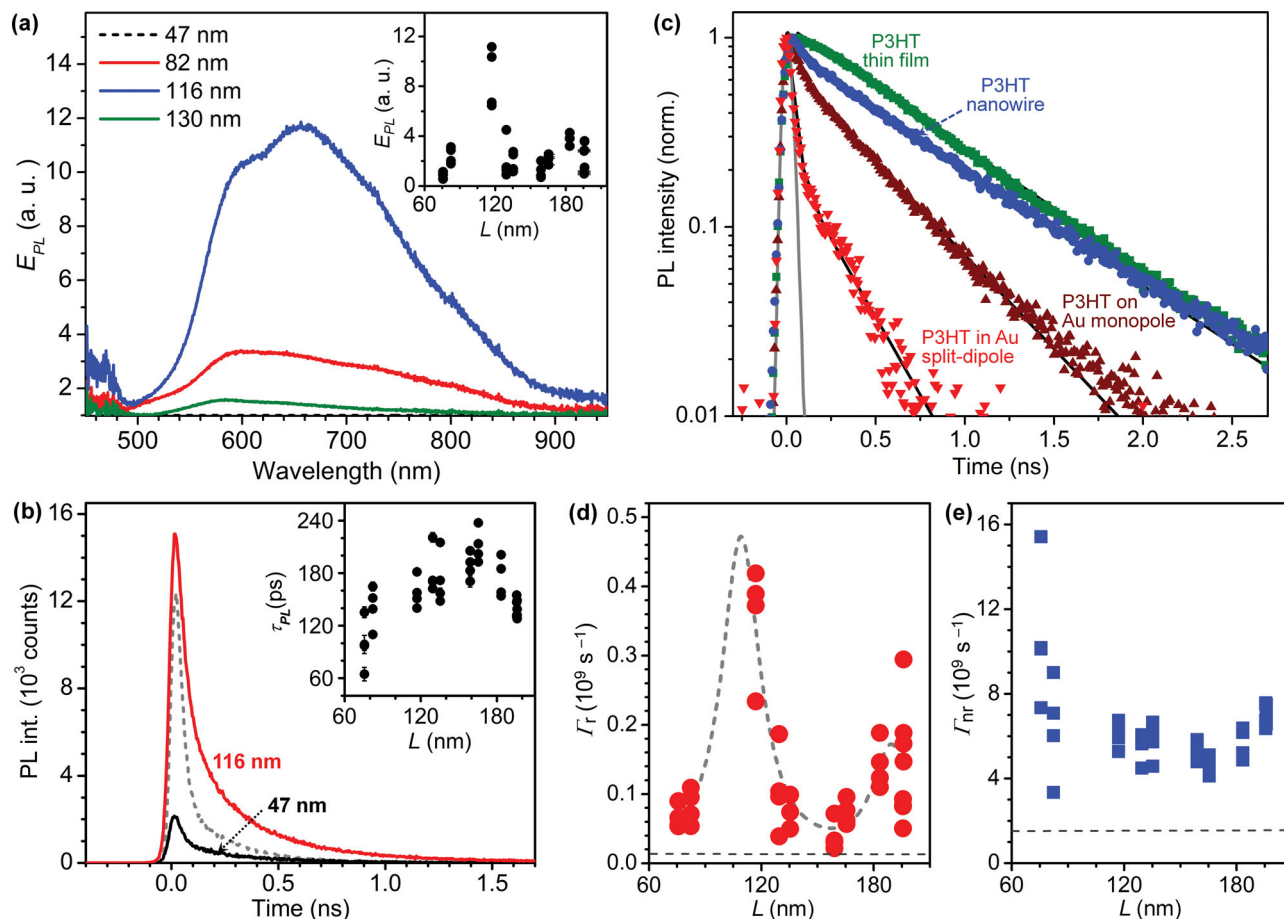


Figure 4. Resonant enhancement of P3HT emission from gold–P3HT–gold split-dipole nanoantennas. a) PL intensity enhancement (E_{PL}) spectra (100 \times oil immersion objective (n.a. = 1.3)) for nanoantenna arrays with L values of 47 ± 7 nm, 82 ± 8 nm, 116 ± 16 nm, and 130 ± 13 nm. Inset in (a): Plot of E_{PL} versus L at a wavelength of 700 nm (4 spectra per L value). b) PL lifetime decays acquired from arrays with average L of 116 nm and 47 nm (collected in the 650 to 750 nm wavelength range), along with a PL lifetime decay from a GaAs nanowire, representing the response of the measurement system. Inset in (b): Total PL lifetime (τ_{PL}) as a function of L (4 measurements per L value). c) PL lifetime decays acquired from a P3HT thin film (green), a neat P3HT nanowire (blue), a single resonant gold-P3HT monomer nanoantenna heterostructure (wine) and a single resonant gold-P3HT-gold split-dipole nanoantenna heterostructure (red). The instrument response function is shown in grey. Solid black lines are exponential fits to the data—the thin film data was fit with a single exponential and all others were fit with a double exponential function. d) Radiative and e) non-radiative decay rates calculated from E_{PL} and τ_{PL} as a function of nanoantenna length (both E_{PL} and τ_{PL} were determined from PL lifetime decays; wavelength range 650–750 nm). The dashed grey lines represent the radiative and non-radiative decay rates of a neat P3HT nanowire. A double-Gaussian function was fit to the data in (d) (black dashed curves).

115 ps, respectively) and P3HT–gold monomer nanoantennas (415 ± 60 ps); Figure 4c. The variation in τ_{PL} for the nanoantennas with L was less apparent than for the intensity enhancement; however, typically, τ_{PL} was ≤ 180 ps where E_{PL} values were highest (Figure 4b, inset). The radiative decay rate was calculated using E_{PL} and τ_{PL} for nanoantennas arrays with different lengths according to the expression:^[8,15,26]

$$\Gamma_r = \Gamma_{PL} E_{PL} \eta_0 \quad (2)$$

where $\Gamma_{PL} = \tau_{PL}^{-1}$ (see SI). Here, E_{PL} was determined from the PL lifetime decays at time = 0 ps for the wavelength range 650–750 nm. For calculation of Γ_r it was assumed that: 1) excitation rate enhancement was negligible (i.e., λ_{ex} is well away from local surface plasmon resonances of the nanoantennas); and 2) PL intensity enhancement was a measure of quantum

efficiency enhancement, i.e., $E_{PL} = \eta_m / \eta_0$.^[12,15,26,27] Note that Γ_r^0 , the radiative decay rate of P3HT in the absence of a resonant nanoantenna was determined from the total PL lifetime value for neat P3HT nanowires according to the expression $\Gamma_r^0 = \eta_0 / \tau_{PL}$. Γ_r^0 was estimated to be $0.014 \times 10^9 \text{ s}^{-1}$; taking $\eta_0 = 1\%$. Values for Γ_r were calculated from Equation 2 and plots of Γ_r and Γ_{nr} versus L are shown in Figure 4d and Figure 4e, respectively (noting that $\Gamma_{nr} = \Gamma_{PL} - \Gamma_r = \Gamma_{nr}^A + \Gamma_{nr}^0$). Γ_r exhibited clear changes with L , reaching values greater than $0.4 \times 10^9 \text{ s}^{-1}$ at $L = 116$ nm and $0.15 \times 10^9 \text{ s}^{-1}$ at $L = 196$ nm (enhancements of 29 and 11, respectively, relative to neat P3HT nanowires). Γ_{nr} of was largest up to $16 \times 10^9 \text{ s}^{-1}$ for short nanoantenna lengths ($L = 76$ nm) and decreased to $\sim 6 \times 10^9 \text{ s}^{-1}$ for larger L (enhancement in Γ_{nr} of ~ 4 relative to that of neat P3HT). These experimentally derived radiative and non-radiative decay rates are in qualitative agreement with those predicted

with simulation in Figure 1, with the radiative decay rate component enhanced periodically with increasing length, and the non-radiative component remaining relatively unchanged. However, both the radiative decay rate enhancement values and the resonance length determined from experiment are significantly smaller than the theoretical values. Many experimental factors are likely to have contributed to these differences including: 1) non-optimal P3HT dipole orientation and variation in the local density of optical states at various locations within the P3HT slot region; 2) deviations in nanoantenna shape from the ideal case (see SI, Figure S4); 3) substrate effects which are likely to increase the effective index of the nanoantennas' environment; 4) bulk array effects (nanoantenna separation distances of between 20 to 60 nm in the arrays are likely to cause a degree of coupling or interference between adjacent nanoantennas); and 5) variation in η_0 . Further investigation of experimental deviations from theory are outside the scope of the current paper but will be considered in more detail in later work on nanoantenna/conjugated polymer hybrid systems.

While $\eta_0 \sim 1\%$ for P3HT, it is important to consider how such a nanoantenna geometry could be applied to other organic semiconductor materials with different η_0 values. The theoretical quantum efficiency enhancement, $E\eta_m$, and η_m are plotted in Figure 5 for a range of η_0 values. It is apparent that higher η_0 results in lower quantum efficiency enhancements (assuming the material has a similar refractive index to P3HT at 700 nm, i.e., ~ 1.4) although modified quantum efficiency can remain large.^[28] Clearly the benefit of the split-dipole nanoantennas in terms of luminescence quantum efficiency applies to materials which possess relatively low η_0 values, but that may have other beneficial properties (such as high organic semiconductor hole mobility, in the case of P3HT). However, the radiative decay rate enhancement can remain high, regardless of the intrinsic

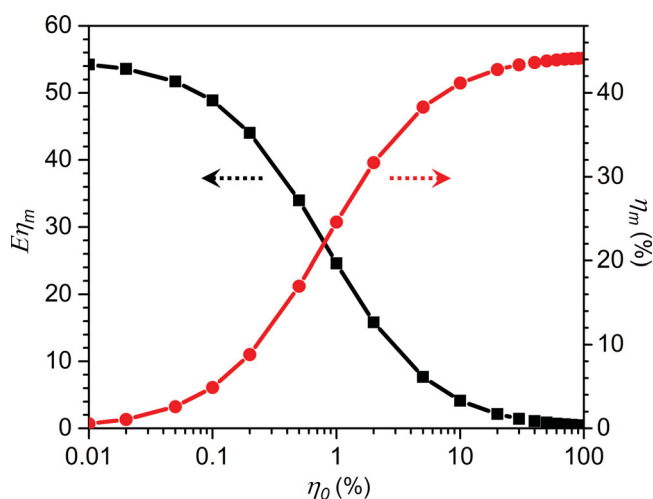


Figure 5. Dependence of modified quantum efficiency on intrinsic emitter quantum efficiency. Theoretical quantum efficiency enhancement, $E\eta_m$ (squares) and modified quantum efficiency, η_m (circles) of a dipole emitter in the slot region of a split-dipole nanoantenna ($L = 180$ nm, $d = 60$ nm, $n_{\text{bk}} = 1.48$ and free-space wavelength is 700 nm) as a function of intrinsic emitter quantum efficiency, η_0 . η_m was calculated from the radiative and total decay rate simulated using 3-dimensional FDTD methods.

quantum efficiency, therefore, where semiconductor radiative emission rate is the critical parameter, e.g., for optical communication or modulation applications, split-dipole plasmonic nanoantennas are attractive rate-enhancement tools. To conclude, this work has implications for a next-generation light-emitting and light-harvesting devices that could incorporate organic semiconductors with intrinsically low quantum efficiency, or for optoelectronic applications where the use of ultra-thin semiconductor material layers (i.e., ≤ 20 nm) would be beneficial.

Experimental Section

Electromagnetic Simulations: Total decay rate was computed using 3D-FDTD software (Lumerical Solutions, Inc.) by integrating the Poynting vector over a closed surface containing only a dipole source, oriented parallel to the antenna long axis, which was embedded in an environment whose wavelength-dependent dielectric constant corresponded to that of P3HT (extracted from Ref. [28]) and which was placed in the slot region of a gold split-dipole nanoantenna ($s = 20$ nm). The entire split-dipole nanoantenna including the P3HT slot containing the dipole source were embedded in a homogeneous environment with refractive index, n_{bk} , of either 1 or 1.48. The radiative decay rate was computed by integrating the Poynting vector over a closed surface incorporating the entire nanoantenna, thereby including non-radiative losses to the metal.^[9,21,22] The non-radiative and radiative decay rate enhancements were calculated by normalizing to those of a dipole emitter in P3HT without the presence of the gold split-dipole nanoantenna. Mesh sizes were ≤ 5 nm for all simulations and, typically, 2 nm for best accuracy. The electromagnetic field intensity within the simulation boundaries was allowed to decay to an intensity of 1×10^{-8} of the original source intensity (which has an intensity value of 1) before simulations were ended, to ensure that simulations had fully converged.

Nanoantenna Fabrication: Split-dipole nanoantennas were fabricated by template-directed sequential electrodeposition of gold and polythiophene in <600 nm thick nanoporous alumina and, subsequent thermal evaporation of gold into the alumina template pores. The typical fabrication route is described as follows. Firstly, aluminum (300–600 nm thick) was thermally evaporated onto a conductive substrate (gold (400 nm)/Al (200 nm)/Si or TiO₂/ITO/glass substrates) typically $2.5 \text{ cm} \times 2.5 \text{ cm}$ square. Copper tape was then applied to the perimeter of the aluminum film to make uniform electrical contact. A strip of copper tape (~ 10 cm long) was then attached to one side of the sample to act as an electrical lead contact to the aluminum during subsequent anodization. Epoxy was then applied to the copper tape on the perimeter of the aluminum film to passivate and expose only the aluminum during anodization. The entire sample was then immersed in oxalic acid (0.3 M; chilled to 4 °C) in a beaker with an aluminum foil counter electrode. A voltage of 35 V was applied to the sample until the entire aluminum layer was anodized (determined by a clear change in appearance to that of the underlying conductive substrate). To remove the alumina barrier layer at the base of the alumina template pores, the sample was immersed in phosphoric acid (5 wt%) for 45 min, after which time the sample was rinsed in deionized water and dried under nitrogen gas flow.

Gold was electrodeposited into the alumina nanopores from gold plating solution (Alfa Aesar) under a pulsed potential of -3 V for a given number of pulses (between 1 and 6, typically) of 0.02 s duration (-0.2 V was applied for 5 s between pulses) using a potentiostat in pulsed chronoamperometry mode. These conditions resulted in gold segment lengths of 27 ± 6 nm per pulse. Up to 12 regions with different gold segment lengths were prepared on a single substrate by carrying out multiple depositions, each time changing the region that was exposed to the electrolyte (by coating the rest of the sample with a removable epoxy) and the number of applied pulses. Platinum mesh was employed as both the counter electrode and the quasi-reference electrode during all electrodepositions.

After gold deposition was completed, the sample was removed from the gold plating solution and was rinsed with deionized water, methanol and IPA and dried under nitrogen gas flow. For deposition of P3HT, 3-hexylthiophene (3HT) monomer (Sigma Aldrich) was electropolymerized at the tips of the electrodeposited gold segments under a pulsed potential of +3 V for 2 pulses, typically (0.02 s duration with -0.6 V applied for 5 s between pulses to discharge the polymer material and allow time for 3HT monomer to diffuse into the nanopores in time for the subsequent applied potential pulse) from a boron trifluoride diethyl etherate ($\text{BF}_3 \cdot \text{O}(\text{C}_2\text{H}_5)_2$) solution (10 g L^{-1}). These conditions resulted in P3HT segment lengths of ~ 10 nm per pulse. Subsequently, the alumina template was rinsed with acetonitrile ($\times 3$; to remove any residual 3HT monomer), acetone, methanol and IPA and dried under nitrogen gas flow.

Finally, to complete the nanoantennas, 40–80 nm of gold was deposited by either thermal or electron-beam evaporation at a rate of 0.6 nm s^{-1} onto the sample. Since the alumina template was thin, the gold was deposited into the template pores onto the P3HT segments, as well as on the surface of the alumina between nanopores. The latter excess gold layer was removed from alumina surface by wiping with a lint-free cloth. To remove the alumina template, the sample was immersed in sodium hydroxide solution (3 M) for 30 min and then rinsed with deionized water and allowed to dry, leaving arrays of nanoantennas oriented vertically on the substrate. To liberate individual nanoantennas, nanoantenna arrays were placed in an eppendorf (1 mL) containing isopropyl alcohol or ethanol (non-solvents for P3HT) and ultrasonication was applied for 1–2 min to disperse the nanoantennas in the liquid. Neat P3HT nanowires were prepared under the same conditions as described above but without the gold electrodeposition or evaporation steps. Gold-P3HT monomer nanoantennas were prepared under similar conditions to the split-dipole nanoantennas but without the gold evaporation step. P3HT thin films were prepared by spin coating from a solution of the polymer (electronic grade; American Dye Source, Inc.) in chloroform (20 g L^{-1}) at 6000 RPM onto a solvent-cleaned glass cover slip. The thickness of the P3HT film was ~ 125 nm (determined by spectroscopic ellipsometry).

Optical Spectroscopy: Prior to optical measurements on nanoantenna arrays, a polyvinyl alcohol layer was deposited on the surface of an array to passivate and prevent photo-oxidation of the semiconductor during photoluminescence measurements. For single nanoantenna measurements, dispersed nanowires were embedded in flexible UV-cured optical epoxy (Norland Optical Adhesive 65, Norland Products, Inc.) and sandwiched between two glass cover slips. Nanoantenna optical measurements were taken on an Axio Observer.Z1 Inverted Microscope (Carl Zeiss, Inc.) equipped with a spectrometer consisting of a 150 mm-focal-length monochromator (slit width $450 \mu\text{m}$, dual turret with 300 g mm^{-1} grating and alignment mirror; SpectraPro 2150i, Princeton Instruments/Acton Research Corp.) and a liquid-nitrogen-cooled CCD camera (1340×100 pixels; Princeton Instruments Spec-10, Roper Scientific, Inc.). For PL lifetime measurements, a 375 nm picosecond laser diode (1.5 mW, 70–300 ps pulse duration depending on laser diode power setting, 40 MHz; LDH-P-C-375B, PicoQuant GmbH) excitation source was used predominantly, as it did not overlap with surface plasmon resonances of the gold nanoantenna but could excite PL emission from P3HT. A picosecond supercontinuum fiber laser ($\sim 2 \text{ mW nm}^{-1}$, 10 ps pulse duration, 455–1750 nm, 40 MHz repetition rate; SC-400-4, Fianium Ltd.) was also employed to access laser excitation wavelengths in the blue and green wavelength range and test the instrument response of the PL lifetime system at different wavelength ranges. For the latter excitation source, a beam sampler (400–700 nm, UV fused silica; BSF10-A1, Thorlabs, Inc.) was used to redirect $\sim 5\%$ of the laser beam to a trigger diode assembly module (TDA 200, PicoQuant GmbH). A <500 nm short-pass filter or a 425–475 nm band-pass filter was placed immediately after the beam sampler at of the output of the supercontinuum laser during PL measurements to restrict the excitation wavelengths at the sample to the absorption band of P3HT. An excitation spot area of approximately $1 \times 10^{-6} \text{ cm}^2$ was typically employed. The

SMA output of the trigger diode assembly module was attached to the input channel of a time-correlated single photon counting (TCSPC) module (PicoHarp 300, PicoQuant GmbH). For 375 nm excitation, the laser diode driver supplied the trigger signal to the TCSPC module. The output of a single photon avalanche diode (SPAD) detector ($50 \mu\text{m}$ active area, <10 dark cps, <50 ps timing resolution; PDM 50T, Micro Photon Devices) was used as the sensing input to the TCSPC module which was interfaced with a computer and controlled with PicoHarp software (PicoQuant GmbH). The instrument response function (IRF) of the PL lifetime system was measured to have a half width of 52 ps, i.e., limited to the temporal resolution of the SPAD detector - at longer wavelengths (425–475 nm using the supercontinuum laser). An IRF of ~ 80 ps was measured at 375 nm (limited by the slightly broader temporal response of the SPAD detector at ultra-violet wavelengths). PL lifetime decays were acquired by placing a beam expander followed by a right-angled mirror, a zero-aperture iris diaphragm (Edmund Optics, Inc.) to select various regions of the sample and an achromatic lens before the SPAD detector which was mounted on an XYZ translation stage. The iris diaphragm was almost fully closed to reject stray light and detect PL from a single nanoantenna, or a particular region of a nanoantenna array of less than $5 \mu\text{m}$ in diameter, at the SPAD. A band-pass filter was used to collect PL lifetime decays integrated over the 650–750 nm wavelength range of P3HT emission. The entire system was aligned to the eyepiece cross hairs of the inverted microscope for accurate repositioning of nanoantennas in the collection path. A $100\times$ oil immersion bright-field objective (numerical aperture of 1.3; Plan-Neofluar, Carl Zeiss, Inc.) was used for both scattered-light and PL spectroscopy. For scattered-light spectroscopy the microscope was operated bright-field reflected light mode with full Köhler illumination for wide-field plane wave excitation the nanowire sample (a variant of the Kretschmann–Raether configuration). A 10 mm fused silica prism (PS610, Thorlabs, Inc.) was placed on top of the sample to allow directly-transmitted (i.e., not scattered) lamp light to pass out of the sample while minimizing back reflection in to the objective at the top glass interface of the sample. Immersion oil (refractive index of 1.518; ImmersolTM 518F, Carl Zeiss, Inc.) was placed between the prism and the top glass substrate, between the microscope slide and the sample and between the oil immersion objective and the bottom glass cover slip of the sample.

Supporting Information

Supporting Information is available from the Wiley Online Library or from the author.

Acknowledgements

This work was supported by the DOE Office of Basic Energy Sciences “Light-Materials Interactions in Energy Conversion” Energy Frontier Research Center under grant DE-SC0001293 (D.M.C., H.A.A.), and also by the Air Force Office of Scientific Research under grant FA9550-09-1-0673 (J.S.F.). D.M.O’C. acknowledges support from the 7th European Community Framework Program (ACTOSPEC project; P10F-GA-2008-221230) and Rutgers’ Institute for Advanced Materials, Devices and Nanotechnology. Use of laboratory facilities in the Nanostructures Group at ISIS, University of Strasbourg is gratefully acknowledged. Useful and supportive discussions with Carrie E. Hofmann, James A. Hutchison, and Shannon W. Boettcher during the course of this work are gratefully acknowledged.

Received: September 3, 2011

Revised: November 29, 2011

Published online:

- [1] I. Gontijo, M. Boroditsky, E. Yablonovitch, S. Keller, U. K. Mishra, S. P. DenBaars, *Phys. Rev. B* **1999**, *60*, 11564.
- [2] J. Vučković, M. Lončar, A. Scherer, *IEEE J. Quantum Electron.* **2000**, *36*, 1131.
- [3] S. McDaniel, S. Blair, *Opt. Express* **2010**, *18*, 17477.
- [4] E. Cubukcu, E. A. Kort, K. B. Crozier, F. Capasso, *Appl. Phys. Lett.* **2006**, *89*, 093120.
- [5] M. Westphalen, U. Kreibig, J. Rostalski, H. Lüth, D. Meissner, *Sol. Energy Mater. Sol. Cells* **2000**, *61*, 97.
- [6] H. A. Atwater, A. Polman, *Nat. Mater.* **2010**, *9*, 205.
- [7] P. Mühlischlegel, H.-J. Eisler, O. J. F. Martin, B. Hecht, D. W. Pohl, *Science* **2005**, *308*, 1607.
- [8] P. Bharadwaj, L. Novotny, *Opt. Express* **2007**, *15*, 14266.
- [9] L. Rogobete, F. Kaminski, M. Agio, V. Sandoghdar, *Opt. Lett.* **2007**, *32*, 1623.
- [10] G. Pellegrini, G. Mattei, P. Mazzoldi, *Nanotech.* **2009**, *20*, 065201.
- [11] A. Alù, N. Engheta, *Nat. Photon.* **2008**, *2*, 307.
- [12] M. Ringler, A. Schwemer, M. Wunderlich, A. Nichtl, K. Kürzinger, T. A. Klar, J. Feldmann, *Phys. Rev. Lett.* **2008**, *100*, 203002.
- [13] T. H. Taminiau, F. D. Stefani, F. B. Segerink, N. F. Van Hulst, *Nat. Photon.* **2008**, *2*, 234.
- [14] D. Gérard, J. Wenger, N. Bonod, E. Popov, H. Rigneault, F. Mahdavi, S. Blair, J. Dintinger, T. W. Ebbesen, *Phys. Rev. B* **2008**, *77*, 045413.
- [15] A. Kinkhabwala, Z. Yu, S. Fan, Y. Avlasevich, K. Müllen, W. E. Moerner, *Nat. Photon.* **2009**, *2*, 654.
- [16] A. G. Curto, G. Volpe, T. H. Taminiau, M. P. Kreuzer, R. Quidant, N. F. van Hulst, *Science* **2010**, *329*, 930.
- [17] J. D. Kraus, R. J. Marhefka, *Antennas for All Applications*, 3rd Edition, McGraw-Hill, New York, USA **2002**.
- [18] K. M. Coakley, B. S. Srinivasan, J. M. Ziebarth, C. Goh, Y. Liu, M. D. McGehee, *Adv. Funct. Mater.* **2005**, *15*, 1927.
- [19] N. C. Greenham, I. D. W. Samuel, G. R. Hayes, R. T. Phillips, Y. A. R. R. Kessener, S. C. Moratti, A. B. Holmes, R. H. Friend, *Chem. Phys. Lett.* **1995**, *241*, 89.
- [20] J. Piris, T. E. Dykstra, A. A. Bakulin, P. H. M. van Loosdrecht, W. Knulst, M. Tuan Trinh, J. M. Schins, L. D. A. Siebbeles, *J. Phys. Chem. C* **2009**, *113*, 14500.
- [21] A. Mohammadi, V. Sandoghdar, M. Agio, *New J. Phys.* **2008**, *10*, 105015.
- [22] D. M. O'Carroll, C. E. Hofmann, H. A. Atwater, *Adv. Mater.* **2010**, *22*, 1223.
- [23] C. A. Foss, G. L. Hornyak, J. A. Stockert, C. R. Martin, *J. Phys. Chem.* **1992**, *96*, 749.
- [24] C. K. Preston, M. Moskovits, *J. Phys. Chem.* **1993**, *97*, 8495.
- [25] M. Schierhorn, S. W. Boettcher, S. Kraemer, G. D. Stucky, M. Moskovits, *Nano. Lett.* **2009**, *9*, 3262.
- [26] E. Dulkeith, A. C. Morteaux, T. Niedereichholz, T. A. Klar, J. Feldmann, S. A. Levi, F. C. J. M. van Veggel, D. N. Reinhoudt, M. Möller, D. I. Gittins, *Phys. Rev. Lett.* **2002**, *89*, 203002.
- [27] O. L. Muskens, V. Giannini, J. A. Sánchez-Gil, J. Gómez Rivas, *Nano Lett.* **2007**, *7*, 2871.
- [28] R. Jansson, H. Arwin, G. Gustafsson, O. Inganäs, *Synth. Met.* **1989**, *28*, C371.